



Cite this: *RSC Sustainability*, 2025, **3**, 2273

## Continuous flow production of $\gamma$ -valerolactone from methyl-levulinate promoted by MOF-derived $\text{Al}_2\text{O}_3\text{-ZrO}_2\text{/C}$ catalysts†

Marina Ronda-Leal,<sup>a</sup> Alina M. Balu,<sup>a</sup> Rafael Luque,<sup>ID</sup><sup>bc</sup> Francesco Mauriello,<sup>ID</sup><sup>d</sup> Alberto Ricchebuono,<sup>ID</sup><sup>ef</sup> Christophe Len,<sup>ID</sup><sup>g</sup> Antonio A. Romero,<sup>ID</sup><sup>a</sup> and Emilia Paone<sup>ID</sup><sup>\*df</sup>

This study investigates the catalytic transfer hydrogenation (CTH) of methyl levulinate (ML) into  $\gamma$ -valerolactone (GVL) using mixed metal oxides derived from metal-organic frameworks (MOFs) under continuous flow conditions. A series of MOF-derived  $\text{Al}_2\text{O}_3\text{-ZrO}_2\text{/C}$  catalysts with different Al/Zr molar ratios were investigated, revealing a synergistic effect that significantly enhances catalytic efficiency. Physico-chemical characterization demonstrates that the incorporation of aluminum into zirconium dioxide increases the surface area as well as the presence of catalytically active acid and basic sites, which are essential for the efficient transfer hydrogenation of ML into GVL.  $\text{Al}_2\text{O}_3\text{-ZrO}_2\text{/C}$  (1 : 1) exhibited the highest ML conversion rate (80%) and GVL yield (72%) at 200 °C within 30 minutes. The study also emphasizes the critical role of reaction parameters in maximizing GVL production. The stability and reusability of the  $\text{Al}_2\text{O}_3\text{-ZrO}_2\text{/C}$  (1 : 1) catalyst, following appropriate thermal treatment, were also assessed.

Received 13th December 2024  
Accepted 6th March 2025

DOI: 10.1039/d4su00797b  
rsc.li/rscsus

### Sustainability spotlight

The production of  $\gamma$ -valerolactone (GVL), a renewable bio-based chemical and fuel additive, plays a crucial role in achieving Sustainable Development Goal 7 (SDG 7) by fostering affordable and clean energy solutions. This study highlights a novel approach using MOF-derived  $\text{Al}_2\text{O}_3\text{-ZrO}_2\text{/C}$  catalysts to produce GVL through a scalable and highly efficient process. By replacing precious metals with cost-effective and sustainable catalysts, this method reduces dependence on non-renewable resources, directly supporting SDG 12 by promoting responsible consumption and production. Furthermore, the integration of renewable feedstocks and the optimization of catalyst reusability minimize environmental impacts, aligning with SDG 13 by contributing to climate action. These advancements underscore the potential of this process to drive greener industrial practices and accelerate the shift towards a circular, low-carbon economy.

## Introduction

The transition towards renewable energy sources, combined with the adoption of circular economy principles, serves as a critical strategy in promoting sustainable development. This approach emphasizes effective resource management by

minimizing environmental impacts and maximizing economic benefits through the reuse, recycling, and regeneration of materials.<sup>1–3</sup> The shift towards these practices necessitates innovative technological advancements, particularly in catalysis, which plays a vital role as a key technology that facilitates the efficient and selective conversion of renewable resources into valuable products.<sup>4,5</sup> One promising direction in achieving circularity and sustainability is the use of lignocellulosic biomass as a renewable feedstock for producing fuels, chemicals, and materials.<sup>6–11</sup> Biomass-derived levulinic acid and its alkyl esters can be utilized to synthesize value-added chemicals, including  $\gamma$ -valerolactone (GVL).<sup>12,13</sup> GVL, recognized for its degradability, non-toxicity, and potential as a green solvent and fuel additive, highlights the necessity for sustainable and economically viable production processes.<sup>14</sup>

An effective method to produce GVL from levulinate is the catalytic transfer hydrogenation (CTH) process, employing H-donor solvents as an indirect hydrogen source, thus addressing challenges linked with the direct use of molecular  $\text{H}_2$ , such

<sup>a</sup>Departamento de Química Orgánica, Universidad de Córdoba, Ctra Nnal IV-A, Km 396, E14014, Córdoba, Spain

<sup>b</sup>Universidad ECOTEC, Km 13.5 Samborondón, Samborondón, EC092302, Ecuador

<sup>c</sup>National University of Science and Technology Politehnica Bucharest, 1-7 Gh Polizu Street, Bucharest, Romania

<sup>d</sup>Dipartimento DICEAM, Università degli Studi Mediterranea di Reggio Calabria Loc. Feo di Vito, I-89122 Reggio Calabria, Italy. E-mail: emilia.paone@unirc.it

<sup>e</sup>Dipartimento di Chimica, INSTM and NIS Centre, Università di Torino, Via Quaranta 15, I-10135 Torino, Italy

<sup>f</sup>Consorzio Interuniversitario per la Scienza e la Tecnologia dei Materiali (INSTM), 50121 Firenze, Italy

<sup>g</sup>Institute of Chemistry for Life and Health Sciences, Chimie ParisTech, PSL Research University, Paris, France

† Electronic supplementary information (ESI) available. See DOI: <https://doi.org/10.1039/d4su00797b>



as purchase, transportation and safety risks, thereby enhancing the sustainability of industrial processes.<sup>15–20</sup>

To reduce the reliance on conventional noble metal-based catalysts for the production of  $\gamma$ -valerolactone (GVL) from alkyl levulinate,<sup>15–17</sup> several non-precious metals have been investigated.<sup>21–25</sup> In this context,  $\text{ZrO}_2$ -based catalysts have emerged as promising non-precious metal alternatives in these reactions. These catalysts, often part of bifunctional catalytic systems that incorporate metals like zirconium (Zr) and niobium (Nb), along with Brønsted and Lewis acid sites, are effective in converting C5 carbohydrates and alcohols into alkyl levulinate.<sup>26–30</sup>

Furthermore, mixed metal oxides are favored in heterogeneous catalysis due to their cost-effectiveness, regenerative capabilities, and superior physical-chemical properties, which include enhanced surface area and thermal stability.<sup>31,32</sup> Recent studies have demonstrated that the coexistence of acid and basic sites in catalysts like  $\text{ZrO}_2$  and  $\text{Al}_2\text{O}_3$  can synergistically improve catalytic performance in MPV reactions.<sup>33,34</sup>

Accordingly, metal-organic frameworks (MOFs) have attracted significant attention as catalytic systems, due to their tunable properties and extensive surface area.

Among their advantages, the porous structure enables the encapsulation of active compounds that act as catalytic sites, thereby offering enhanced stability and selectivity in heterogeneous catalysis. These features facilitate efficient and selective conversion of lignocellulosic biomass.<sup>39–44</sup> While MOFs have demonstrated proven efficacy under liquid batch conditions, their application in continuous flow systems poses challenges, primarily due to their structural instability and leaching during chemical reactions.<sup>45</sup> Nevertheless, MOFs can be effectively utilized as templates to create MOF-derived catalysts.<sup>46–51</sup> Their porous structure enables the encapsulation of active compounds that act as catalytic sites, thereby offering enhanced stability and selectivity in catalysis. During this templating process, calcination plays a crucial role in removing the organic

ligands from the MOF structure.<sup>52</sup> This leaves behind metal oxide nanoparticles or clusters, which further contributes to the stabilization of the catalyst structure. The addition of new properties to the material could address the challenges associated with MOF-flow systems that have been previously reported and may also enhance the batch catalytic performance of both MOFs and MOF-derived oxides. Several studies have already reported the use of MOF-derived catalysts in catalytic reactions for the production of GVL under batch conditions *i.e.*  $\text{Ru-ZrO}_2@C$ ,<sup>53</sup>  $\text{Ir}@\text{ZrO}_2@C$ ,<sup>54</sup> and  $\text{Ru}@\text{C-Al}_2\text{O}_3$ .<sup>55</sup> However, these materials contain noble metals. On the other hand, flow-catalytic reactions from methyl levulinate to GVL have been studied (Table 1) in some research.

Our study investigates the use of MOF-derived  $\text{Al}_2\text{O}_3-\text{ZrO}_2/C$  catalysts for converting methyl levulinate into GVL under continuous flow conditions, focusing on the effect of varying Al/Zr molar ratios on catalytic efficiency and selectivity. By enhancing the selectivity for GVL production, a potential green fuel, this research advances the development of highly active non-noble metal catalysts and promotes sustainable catalytic processes.

## Experimental section

### Synthetic procedures

All chemicals were acquired as analytical grade compounds from commercial sources and used without any further purification: terephthalic acid (>99%, Acros), zirconium(IV) chloride ( $\text{ZrCl}_4$ ) (>99.9%, Sigma-Aldrich), aluminum nitrate nonahydrate ( $\text{Al}(\text{NO}_3)_3 \cdot 9\text{H}_2\text{O}$ ) (>99%, Merck), methanol (MeOH) (>99.9%, Panreac), *N,N*-dimethylformamide (DMF) (>99.9%, Panreac), methyl levulinate (>98%, Sigma-Aldrich), and isopropanol (>99.9%, Panreac).

Bimetallic MOFs, utilizing  $\text{UiO-66}$  (Zr) and  $\text{MIL-53}$  (Al) as sacrificial templates, were prepared for a series of  $\text{Al}_2\text{O}_3-\text{ZrO}_2/C$  catalysts with varying Al/Zr ratios (0 : 1; 1 : 2; 1 : 1; 2 : 1). The preparation began with solution A, consisting of terephthalic

Table 1 Catalyst and conditions used for production of GVL under flow conditions

Catalyst	Conditions	Conversion (%)	Selectivity (%)	Ref.
$\text{ZrO}_2$	ML : 2-PrOH = 1 : 10 (molar ratio), $\tau = 1$ s, % mol $\text{N}_2$ : ML : EtOH = 90.1 : 0.9 : 9, 250 °C	>99	80	35
$\text{UiO-66}$ (Zr)	ML : 2-PrOH = 1 : 5.4 (molar ratio), time on stream: 1 h, 240 °C	>99	74	36
5% Ru/C	ML : 2-PrOH 1 : 50, 20 bar, 0.4 mL min <sup>-1</sup> , 150 °C	>95	85	37
Zr10/HBEA (75)	0.3 M methyl levulinate and 0.01 M pyridine in 2-propanol, flow rate of 0.2 mL min <sup>-1</sup> , at 200 °C and 30 bar pressure	45.5	96	38
$\text{Al}_2\text{O}_3-\text{ZrO}_2/C$	ML : 2PrOH = 1 : 100, flow 0.5 mL min <sup>-1</sup> , 30 bar, 220 °C, 0.5 g cat	>99	85	This work



acid and zirconium chloride in 50 mL of DMF, and solution B, consisting of terephthalic acid and aluminum nitrate in 50 mL of DMF. Initially, terephthalic acid was added to zirconium chloride with 50 mL of DMF (solution A) and mixed until it formed a clear solution over 30 minutes. Concurrently, terephthalic acid was mixed with aluminum nitrate in an equal volume of DMF (solution B) for another 30 minutes. Subsequently, solution A was added to solution B under stirring for 1 hour, during which the ratios of Al to Zr were adjusted. The combined solution was then transferred to a 125 mL stainless steel-lined Teflon autoclave and heated at 120 °C for 24 hours. The resultant precipitate was filtered and washed several times with DMF and MeOH. Finally, the precipitate was dried overnight at 80 °C and pyrolyzed in a muffle furnace under a mixed atmosphere (N<sub>2</sub>/air) at 600 °C for 2 hours.

## Methodology

The crystal structure and phase composition of the synthesized Al<sub>2</sub>O<sub>3</sub>–ZrO<sub>2</sub>/C catalysts were characterized using a Bruker D8 DISCOVER with Cu Ka radiation ( $l = 1.5418 \text{ \AA}$ ) and operated at a scanning speed of 1° min<sup>-1</sup> over a range from 5° to 80° 2 $\theta$ . The textural properties of the samples were examined using physisorption isotherms with N<sub>2</sub>, measured on a Micromeritics ASAP 2000 at 77 K. Samples were degassed under a vacuum of 0.1 Pa for 24 h at 130 °C prior to measurement.

The crystal structure and phase composition of the synthesized Al<sub>2</sub>O<sub>3</sub>–ZrO<sub>2</sub>/C catalysts were characterized using a Bruker D8 DISCOVER with Cu Ka radiation ( $l = 1.5418 \text{ \AA}$ ) and operated at a scanning speed of 1° min<sup>-1</sup> over a range from 5° to 80° 2 $\theta$ .

*In situ* IR spectroscopy of adsorbed CO<sub>2</sub> was used to characterize the acidic and basic sites on the surface of the MOF-derived catalysts. Transmission IR spectra were collected using a Bruker Vertex 70 spectrophotometer equipped with a Mercury–Cadmium–Telluride (MCT) cryo-detector in the 4000–600 cm<sup>-1</sup> range with a resolution of 2 cm<sup>-1</sup>. The samples, gently pelletized (applied pressure *ca.* 0.2 Ton per cm<sup>2</sup>) into self-supporting thin pellets (thickness  $\sim$  0.01 mg mm<sup>-2</sup>), were placed in a custom cell, equipped with KBr windows, designed for thermal treatments in a controlled atmosphere. Prior to analysis, the samples were activated on a vacuum line by degassing the pellets at 500 °C (ramp rate 5 °C min<sup>-1</sup>) until the pressure reached  $5 \times 10^{-4}$  mbar, then kept overnight. Hereafter, 100 mbar O<sub>2</sub> was dosed into the cell and maintained for 15 min. This process was repeated three times, followed by a 2 h long outgassing step. Lastly, the cell was cooled down to room temperature and, without exposure to air, connected to a second vacuum line and placed inside the IR spectrometer. Experiments were carried out by sending an initial dose of 25 mbar CO<sub>2</sub> on the catalysts at beam temperature. Spectra were continuously measured for 15 min, allowing the adsorbate–adsorbent system to equilibrate. Finally, the cell was opened to a dynamic vacuum to observe the behaviour of the species formed upon CO<sub>2</sub> adsorption during evacuation at beam temperature. The evolution of the system under these conditions was monitored by collecting IR spectra for an additional 15 min. The collected spectra were *a posteriori* corrected for the sample thickness in order to allow the semi-quantitative considerations.

Surface activity was further studied using pulse chromatographic titration at 200 °C. Pyridine (PY) and 2,6-dimethylpyridine (DMPY) served as titrant bases in a cyclohexane solution using a Hewlett Packard 5890 Series II gas chromatograph. The catalysts were saturated by small injections (2  $\mu\text{L}$  each) of these molecules. The probe molecules were then detected in the GC with an FID detector, assuming that pyridine titrates both Brønsted and Lewis sites, while 2,6-dimethylpyridine selectively titrates Brønsted acid sites.

X-ray photoelectron spectroscopy (XPS) was conducted to analyze the chemical composition of the surface materials. The internal structure of the catalysts was examined using a JEOL JEM-2100F transmission electron microscope (TEM). The same instrument was used for energy-dispersive X-ray (EDX) testing to verify the good dispersion of the MOFs and oxides. Morphological characteristics were assessed through scanning electron microscopy (JEOL JSM 6300), with an energy-dispersive X-ray detector (EDS) used for qualitative analysis of the sample's constituent elements.

Reactions were conducted using a ThalesNano Phoenix continuous flow reactor (see Scheme S1†). The reactor was loaded with 0.5 g of catalyst, packed into a 70 mm long ThalesNano CatCart, and inserted into the reactor. A solution of 0.2 M methyl levulinate in 2-propanol was passed through the CatCart at a flow rate of 0.1 to 0.5 mL min<sup>-1</sup>, under a nitrogen pressure of 30 bar and temperatures ranging from 160 to 220 °C. Samples were collected at specific times on stream; the analyzed samples correspond to the reactor's outlet stream collected over specified intervals. Therefore, the GC results represent an average of the reaction mixture's composition from the start of the reaction up to the respective sampling time.

Product identification was performed by comparing with commercially available samples using an Agilent 7820A GC/5977B equipped with an HP-5ms column (30 m  $\times$  0.25 mm  $\times$  0.25  $\mu\text{m}$ ). Products were quantified using an Agilent 6890A gas chromatograph equipped with an FID detector and a non-polar fused silica hydroxyl column, SUPELCO EQUITY TM-1 (60 m  $\times$  0.25 mm  $\times$  0.25  $\mu\text{m}$ ). The carrier gas used was N<sub>2</sub>, with a flow rate of 1.2 mL min<sup>-1</sup>. The heating program started with a 1 min isotherm at 60 °C, followed by an increase to 180 °C at a rate of 5 °C min<sup>-1</sup>, maintained for 5 min, then increased to 250 °C at a rate of 15 °C min<sup>-1</sup> and maintained for another 5 min.

The methyl levulinate conversion, product selectivity and product yield were calculated as follow:

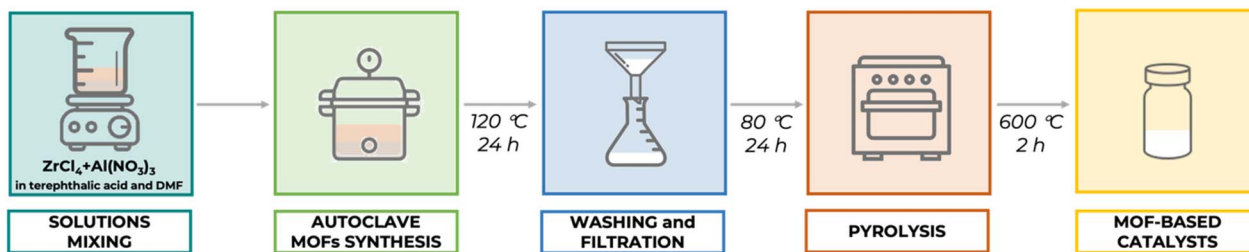
$$\text{Conversion (\%)} = \frac{\text{mol}_{\text{ML initial}} - \text{mol}_{\text{ML final}}}{\text{mol}_{\text{ML initial}}} \times 100 \quad (1)$$

$$\text{Selectivity (\%)} = \frac{\text{mol}_{\text{specific product}}}{\text{sum of mol}_{\text{all products}}} \times 100 \quad (2)$$

$$\text{Yield (\%)} = \frac{\text{mol}_{\text{specific product}}}{\text{mol}_{\text{ML initial}}} \times 100 \quad (3)$$

Carbon balance was assessed by GC-FID quantification, obtaining a loss-value in all cases lower than 2% of carbon loss.





Scheme 1 Schematic representation of the synthesis and preparation process of the bimetallic MOF-derived  $\text{Al}_2\text{O}_3$ – $\text{ZrO}_2$ /C catalysts.

## Results and discussion

### Catalyst synthesis and characterization

MOF-derived  $\text{Al}_2\text{O}_3$ – $\text{ZrO}_2$ /C catalysts were prepared using a solvothermal method as described by McKinstry and colleagues.<sup>56</sup> Briefly, the synthesis involves combining solutions of terephthalic acid with zirconium chloride and/or aluminum nitrate in dimethylformamide (DMF). This mixture is then heated in an autoclave to form the MOF structure. After washing and drying, the material is subjected to pyrolysis in a nitrogen atmosphere to convert the precursors into the desired  $\text{Al}_2\text{O}_3$ – $\text{ZrO}_2$ /C catalysts. A schematic representation of the synthesis and preparation process of the samples is depicted in Scheme 1.

$\text{N}_2$  physisorption was utilized to investigate the textural properties of the catalysts (Table 2). In contrast to the precursor MOFs, which typically exhibit type I isotherms, all catalysts displayed type IV isotherms indicative of mesoporous materials (Fig. S1†). This transformation can be attributed to the removal of organic linkers during MOF calcination, which originally contributed to microporosity. The highest surface area was recorded for  $\text{Al}_2\text{O}_3$ /C at  $232 \text{ m}^2 \text{ g}^{-1}$ , while  $\text{ZrO}_2$ /C exhibited the lowest at  $31 \text{ m}^2 \text{ g}^{-1}$ . Materials containing  $\text{Al}_2\text{O}_3$  in their structure ( $\text{Al}_2\text{O}_3$ – $\text{ZrO}_2$ /C mixtures) demonstrated enhanced  $\text{ZrO}_2$ /C surface areas, mostly in ratios of 1:1 and 1:2. This trend extends to total pore volume and pore diameter, where an increased content of  $\text{Al}_2\text{O}_3$ /C correlates with large total pore volumes and diameters (Table 2).

Oxide crystal structure was investigated by XRD analysis (Fig. 1).  $\text{ZrO}_2$ /C exhibits a mixed phase between monoclinic and tetragonal phases.<sup>35–38,56–60</sup>  $\text{Al}_2\text{O}_3$ /C shows a characteristic amorphous structure.<sup>61</sup> Peaks attributed to monoclinic  $\text{ZrO}_2$ /C appear at 28 (111) and 62 (312)  $2\theta$  degrees while the tetragonal phase appears at 30 (101), 35 (110), 50 (112) and 59 (131)  $2\theta$  degrees. On the other hand, mixed oxide structures combine characteristics from both pure oxides, resulting in materials

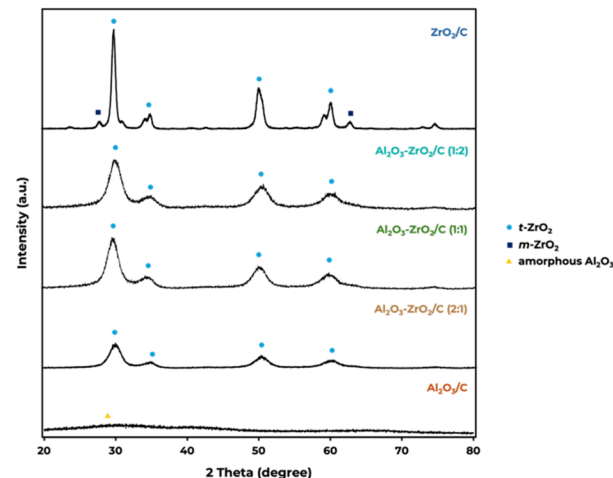


Fig. 1 XRD patterns of calcined MOF-derived  $\text{Al}_2\text{O}_3$ – $\text{ZrO}_2$ /C catalysts.

that exhibit unique properties, leading to a structure more amorphous than pure  $\text{ZrO}_2$ /C due to the presence of  $\text{Al}_2\text{O}_3$ /C. Furthermore, it is noteworthy that these mixed oxide structures tend to maintain the tetragonal phase of  $\text{ZrO}_2$ /C as the predominant phase. Other studies involving the synthesis of these mixed oxides have also shown similar trends.<sup>62</sup>

The acidity of the catalysts was determined through pyridine adsorption followed by titration, with the acid site density results presented in Table 2, normalized for both surface area ( $\text{m}^2$ ) and mass (g). Notable differences were observed in the acid site densities between the pure oxides  $\text{ZrO}_2$ /C and  $\text{Al}_2\text{O}_3$ /C.  $\text{ZrO}_2$ /C, which has a relatively lower specific surface area of  $31 \text{ m}^2 \text{ g}^{-1}$ , demonstrated a higher acid site density of  $1 \mu\text{mol m}^{-2}$ . This is attributed to a more pronounced aggregation of acid sites on the limited surface area available. In contrast,  $\text{Al}_2\text{O}_3$ /C, with a significantly higher specific surface area of  $232 \text{ m}^2 \text{ g}^{-1}$ ,

Table 2 Textural properties of the investigated catalyst

Catalyst	Al/Zr ratio	SA ( $\text{m}^2 \text{ g}^{-1}$ )	$V_{\text{BJH}}$ ( $\text{cm}^3 \text{ g}^{-1}$ )	$V_{\text{MESO}}$ ( $\text{cm}^3 \text{ g}^{-1}$ )	$D_{\text{BJH}}$ ( $\text{\AA}$ )	Total acidity ( $\mu\text{mol m}^{-2}$ )	Total acidity ( $\mu\text{mol g}^{-1}$ )	Brønsted acidity ( $\mu\text{mol DMPY g}^{-1}$ )
$\text{ZrO}_2$ /C	—	31	0.16	0.08	80	1	32	<5
$\text{Al}_2\text{O}_3$ – $\text{ZrO}_2$ /C (1:2)	1:2	165	0.75	0.54	100	0.18	30	<5
$\text{Al}_2\text{O}_3$ – $\text{ZrO}_2$ /C (1:1)	1:1	210	0.85	0.50	100	0.37	77	<5
$\text{Al}_2\text{O}_3$ – $\text{ZrO}_2$ /C (2:1)	2:1	96	0.42	0.21	70	0.26	25	<5
$\text{Al}_2\text{O}_3$ /C	—	232	1.44	0.94	300	0.18	43	<5



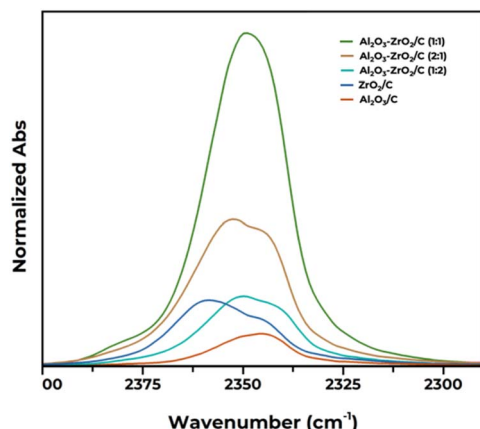


Fig. 2 *In situ* IR spectra of  $\text{CO}_2$  adsorbed on all the pure and mixed oxides recorded at beam temperature. The spectra are corrected for the pellet thickness and focus on the  $2400\text{--}2300\text{ cm}^{-1}$  range, relative to linear  $\text{CO}_2$  complexes.

showed the lowest acid site density of  $0.18\text{ }\mu\text{mol m}^{-2}$ , likely resulting from the broader dispersion of acid sites across the extensive surface. However, when quantified based on the total number of acid centers per gram,  $\text{Al}_2\text{O}_3/\text{C}$ , with  $43\text{ }\mu\text{mol g}^{-1}$ , is comparably effective to  $\text{ZrO}_2/\text{C}$ , which has  $32\text{ }\mu\text{mol g}^{-1}$ . This indicates that the functional performance of  $\text{Al}_2\text{O}_3/\text{C}$  compensates for its lower density per unit area through a greater overall quantity of accessible acid sites.

The mixed oxides exhibit textural properties that represent a balance between the enhanced surface area provided by  $\text{Al}_2\text{O}_3$  and the strong inherent acidity of  $\text{ZrO}_2$ . A tendency was observed, where an excess of either component –  $\text{Al}_2\text{O}_3$  or  $\text{ZrO}_2$  – results in acid site densities ( $\mu\text{mol g}^{-1}$ ) similar to those of the individual oxides. The optimal acid site density was observed in the  $\text{Al}_2\text{O}_3\text{--ZrO}_2/\text{C}$  (1:1) catalyst, achieving the highest values both per gram ( $77\text{ }\mu\text{mol g}^{-1}$ ) and per unit area ( $0.37\text{ }\mu\text{mol m}^{-2}$ ).

Furthermore, it is important to note that all materials predominantly exhibit Lewis acid sites, with the absence of Brønsted acid sites. This characterization underscores the Lewis acid sites as the primary contributors to the acidity of these catalysts.

To further elucidate the acid–base properties of the materials, we added  $\text{CO}_2$  as a probe molecule in this study. This approach allows the simultaneous assessment of the materials' acidic and basic characteristics, contributing to a more complete understanding of their catalytic properties. Following this line, an *in situ* IR study exploiting  $\text{CO}_2$  as a probe molecule was performed to characterize the acid and basic sites on the surface of the catalysts. Two spectral regions were analyzed separately: (i) acid site region (within the  $2400\text{--}2300\text{ cm}^{-1}$  range), where the adsorption bands are ascribed to the  $\Sigma_u^+$  mode of  $\text{CO}_2$  linearly adsorbed on cationic sites, responsible for Lewis acidity,<sup>63–66</sup> and (ii) basic site region (within the  $1800\text{--}1200\text{ cm}^{-1}$  range), where the adsorption bands are ascribed to carbonate and bicarbonate species (unidentate, bidentate, or

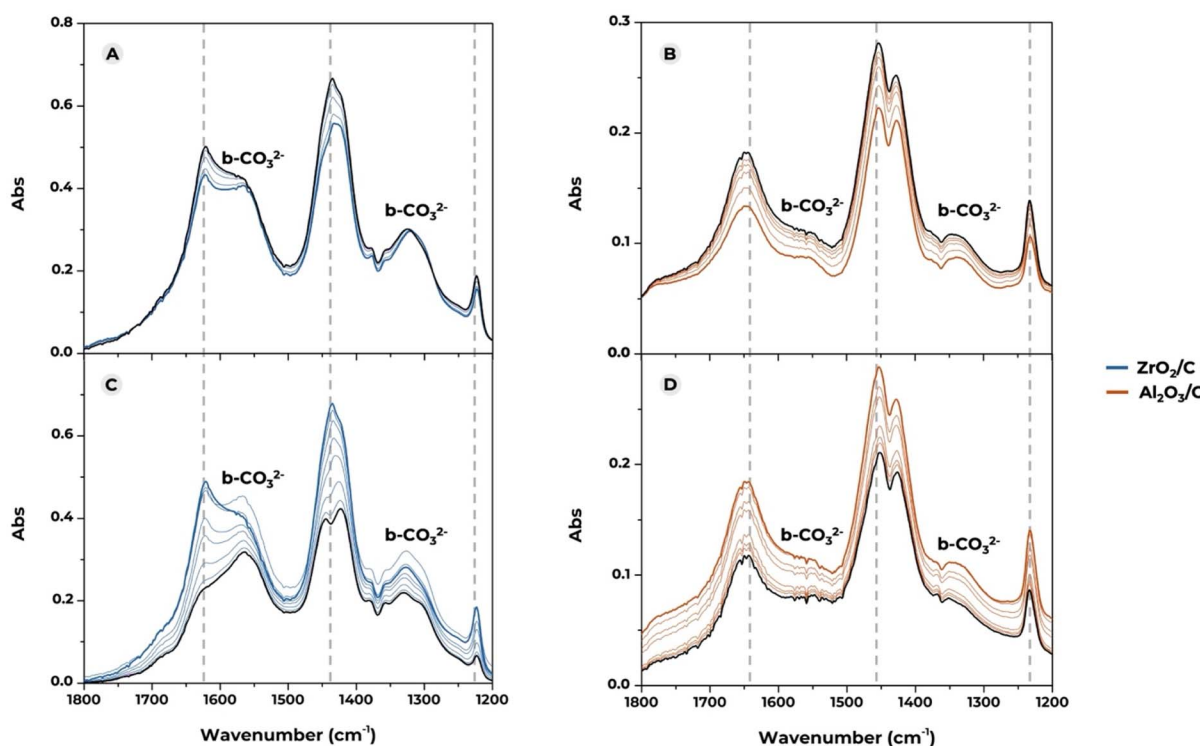


Fig. 3 The *in situ* IR spectra of  $\text{CO}_2$  adsorption in the  $1800\text{--}1200\text{ cm}^{-1}$  range are divided into two sections. Sections (A) and (B) correspond to the stabilization of the carbonate species on the surface of  $\text{ZrO}_2$  (A) and  $\text{Al}_2\text{O}_3$  (B) in contact with  $25\text{ mbar}$   $\text{CO}_2$  (0 min corresponding to the blue and orange bold spectra and 15 min to the black bold spectra). Sections (C) and (D) follow the  $\text{CO}_2$  degassing step on the same materials (0 min corresponding to the blue and orange bold spectra and 15 min to the black bold spectra).



bridged bidentate) formed after the adsorption of  $\text{CO}_2$  on electron-rich oxygen atoms on the surface.<sup>65,67,68</sup>

Fig. 2 reports the IR spectra in the 2400–2300  $\text{cm}^{-1}$  region, relative to the linear adsorption of  $\text{CO}_2$  on Lewis acid sites. In agreement with the existing literature, the overall absorption of  $\text{CO}_2$  on  $\text{ZrO}_2/\text{C}$  is shifted towards higher wavenumbers than on  $\text{Al}_2\text{O}_3/\text{C}$ , indicating that the acid sites on the surface of the former material are generally stronger than the ones on the latter. The spectra of  $\text{CO}_2$  on both  $\text{ZrO}_2/\text{C}$  and  $\text{Al}_2\text{O}_3/\text{C}$  can be decomposed into 2–3 contributions, suggesting the presence of at least a few different families of acid sites on each material, as previously reported.<sup>67,69</sup> Mixed oxides also show distinct contributions centered at intermediate wavenumbers between pure  $\text{Al}_2\text{O}_3/\text{C}$  and  $\text{ZrO}_2/\text{C}$  due to which unambiguous assignation to  $\text{CO}_2$  adsorption on  $\text{Al}^{3+}$  or  $\text{Zr}^{4+}$  is not straightforward. The intensity of the overall band in the thickness-corrected spectra can be correlated with the abundance of the acid sites, pointing out substantial differences in the inspected materials. Pure oxides demonstrate lower acidity compared to some mixed oxides, such as  $\text{Al}_2\text{O}_3\text{-ZrO}_2/\text{C}$  (1 : 1) and  $\text{Al}_2\text{O}_3\text{-ZrO}_2/\text{C}$  (2 : 1). Results are in line with those in Table 2 obtained using pyridine, confirming the equimolar mixture of  $\text{Al}_2\text{O}_3\text{-ZrO}_2/\text{C}$  (1 : 1) as the material with the highest abundance of Lewis acid sites.

Fig. 3 presents the IR spectra in the 1800–1200  $\text{cm}^{-1}$  region, recorded to follow the adsorption of  $\text{CO}_2$  on the basic sites of the pure  $\text{ZrO}_2/\text{C}$  and  $\text{Al}_2\text{O}_3/\text{C}$ , which serve as references for the mixed materials. The measurements are divided into two sections. Spectra in Fig. 3A and B are meant to follow the evolution of the carbonate species formed upon  $\text{CO}_2$  adsorption under static conditions. The blue and orange spectra in Fig. 3A and B were collected immediately after  $\text{CO}_2$  dosing (25 mbar), while the black spectra correspond to the final situation, obtained after waiting 15 minutes maintaining the same  $\text{CO}_2$  pressure. Spectra in Fig. 3C and D are recorded degassing  $\text{CO}_2$  under dynamic vacuum. The blue and orange spectra in Fig. 3C and D were collected immediately after exposing the sample to dynamic vacuum, while the black spectra were collected after a degassing of 15 minutes.

Dotted vertical lines mark the positions of bicarbonate species ( $\text{HCO}_3^{2-}$ )

- Symmetric C–O stretching ( $\nu_{\text{sym}}$  C–O) at 1435–1480  $\text{cm}^{-1}$ . The band features contributions from monodentate (1435  $\text{cm}^{-1}$ ) and bidentate bicarbonates (1455  $\text{cm}^{-1}$ ), complicating the analysis.

- Asymmetric C–O stretching ( $\nu_{\text{asym}}$  C–O) at 1660–1680  $\text{cm}^{-1}$
- Bending of the OH group (dOH) on bicarbonate species at 1230  $\text{cm}^{-1}$ .

Conversely, the bands centered at  $\sim$ 1550  $\text{cm}^{-1}$  and  $\sim$ 1330  $\text{cm}^{-1}$  indicate the presence of bidentate carbonates, as confirmed by the significant spectral separation ( $D_v = 200 \text{ cm}^{-1}$ ).<sup>60,65,66</sup>

By comparing the spectra of the carbonate species formed on the surface of the two pure oxides, it emerges that  $\text{ZrO}_2/\text{C}$  exhibits a strong affinity for  $\text{CO}_2$ , forming both carbonates and bicarbonates. On the other hand, the spectra recorded on  $\text{Al}_2\text{O}_3/\text{C}$  present a much smaller contribution of carbonate bands, suggesting that the basicity profile of  $\text{Al}_2\text{O}_3/\text{C}$  is primarily provided by OH groups, which is in line with previous studies.<sup>70</sup>

Fig. 4 presents the thickness-corrected spectra of the five catalysts, with pure materials shown in Fig. 4A and mixed materials in Fig. 4B. All spectra are normalized and displayed on a consistent scale to simplify comparison. Two spectra, one recorded after contact with  $\text{CO}_2$  (solid line) and one upon degassing at room temperature (dotted line), are reported for each catalyst. In both cases, the reported spectrum corresponds to the situation after 15 minutes of equilibration and degassing, respectively. The overall higher intensity of the bands in the  $\text{ZrO}_2/\text{C}$  spectrum compared with  $\text{Al}_2\text{O}_3/\text{C}$  indicates the higher basicity of the former pure catalyst (Fig. 4A).<sup>71</sup> Regarding the mixed samples, it is evident that  $\text{Al}_2\text{O}_3\text{-ZrO}_2/\text{C}$  (1 : 1) exhibits the highest abundance of basic sites (even compared with the pure  $\text{ZrO}_2/\text{C}$ ). The other mixed oxides display similar basicity to one another, although the formed species are different due to the varying  $\text{Al}_2\text{O}_3\text{-ZrO}_2$  molar ratios.<sup>72–75</sup>

Lastly, the dotted spectra in Fig. 4 allow the stability of the carbonate species to be assessed depending on the quantity that

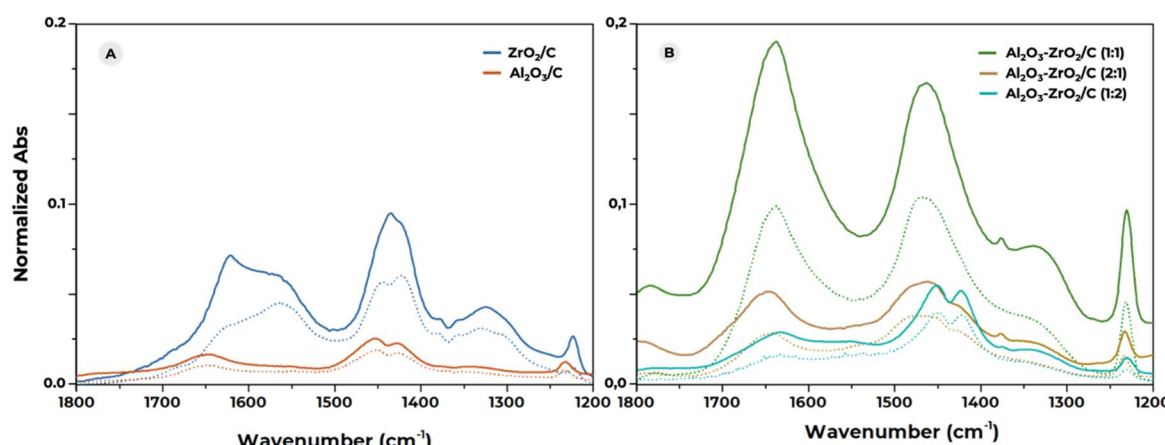


Fig. 4 IR spectra of  $\text{CO}_2$  adsorption of pure oxides (A) and mixed oxides (B) with the solid lines corresponding to stabilization of 25 mbar  $\text{CO}_2$  and dotted lines to  $\text{CO}_2$  outgassing ( $5 \times 10^{-5}$  mbar).



Table 3 XPS binding energies of the C 1s, O 1s, Zr 3d, and Al 2p core levels of the bimetallic MOF-derived  $\text{Al}_2\text{O}_3$ – $\text{ZrO}_2$ /C catalysts

Sample	Binding energy (eV)					
	O 1s		Al 2p		Zr 3d	
	$\text{Al}_2\text{O}_3$	$\text{C}=\text{O}/\text{C}-\text{O}$	$\text{ZrO}_2$	$\text{Al}_2\text{O}_3$	$\text{ZrO}_2$	$\text{Zr}(\text{OH})_2$
$\text{ZrO}_2/\text{C}$	—	—	529.9	—	181.8–184.1	183.2–185.4
$\text{Al}_2\text{O}_3$ – $\text{ZrO}_2/\text{C}$ (1 : 2)	533	531.9–530.8	530.7	75.2–73.7	181.8–184.1	183.2–185.4
$\text{Al}_2\text{O}_3$ – $\text{ZrO}_2/\text{C}$ (1 : 1)	533	531.9–530.8	530.7	75.2–73.7	181.8–184.1	183.2–185.4
$\text{Al}_2\text{O}_3$ – $\text{ZrO}_2/\text{C}$ (2 : 1)	533	531.9–530.8	530.7	75.2–73.7	181.8–184.1	183.2–185.4
$\text{Al}_2\text{O}_3/\text{C}$	533	—	—	75.2–73.7	—	—

is retained after the degassing treatment at room temperature. The IR bands of the carbonate species decrease in intensity in all cases upon degassing, with the  $\text{Al}_2\text{O}_3$ – $\text{ZrO}_2/\text{C}$  (1 : 1) catalyst being able to retain the highest quantity of carbonates compared with the rest of the materials for the same degassing time.

X-ray Photoelectron Spectroscopy (XPS) was employed to characterize the surface chemical composition of the catalysts under investigation. Detailed binding energies for the O 1s, Al 2p, and Zr 3d orbitals are reported in Table 3 across all samples. For the  $\text{Al}_2\text{O}_3/\text{C}$  and  $\text{ZrO}_2/\text{C}$  samples, the binding energies observed for O 1s, Al 2p, and Zr 3d are consistent with established signatures for  $\text{Al}_2\text{O}_3$  and  $\text{ZrO}_2$  oxides, respectively. In mixed  $\text{Al}_2\text{O}_3$ – $\text{ZrO}_2/\text{C}$  samples, the O 1s spectrum exhibits a broad peak at 529.7 eV, reflecting contributions from oxygen in both  $\text{Al}_2\text{O}_3$  and  $\text{ZrO}_2$  matrices, and at 530.8 eV, indicative of oxide defects. Additional contributions are noted at 531.5 eV and 533 eV, corresponding to carbonyl groups and ether linkages or possibly to water adsorbed on the surface. The Al 2p core-level spectra of these catalysts display peaks at approximately 73.7 and 75.2 eV, indicative of  $\text{Al}^{3+}$  in distinct chemical environments. The peak at 73.7 eV is attributed solely to  $\text{Al}_2\text{O}_3$ , while the peak at 75.2 eV is likely associated with hydrated aluminum oxides or hydroxide species. Similarly, Zr 3d core-level spectra show peaks with a separation of 2.4 eV, typical for  $\text{ZrO}_2$ , at binding energies of 184.1 and 181.8 eV. Additional peaks at 185.4 eV and 183.2 eV are identified as originating from  $\text{Zr}(\text{OH})_2$ . These observations align with the known characteristics of  $\text{ZrO}_2$  derived from UiO-66 (Zr), underscoring the intricate composition of these catalytic materials.<sup>75</sup>

An increase in the Zr binding energy was noted, suggesting that Zr and Al species are effectively dispersed within the mixed metal oxides corroborated by Energy Dispersive X-ray Spectroscopy (XPS) analysis (Fig. S2†). The positive charge on Zr atoms, attributable to the higher electronegativity of Al in Zr–O–Al bonds, likely enhances the number and efficacy of Lewis acid sites. This phenomenon is in agreement with previously reported literature findings.<sup>75</sup>

Transmission electron microscopy (TEM) analysis was carried out to elucidate the size and morphology of the catalyst structures. The  $\text{Al}_2\text{O}_3$ – $\text{ZrO}_2/\text{C}$  (1 : 1) sample displays aggregates of small particles, creating interparticle voids that contribute to a disordered structure (Fig. 5). This observation is consistent with the X-ray diffraction (XRD) results presented in Fig. 1.

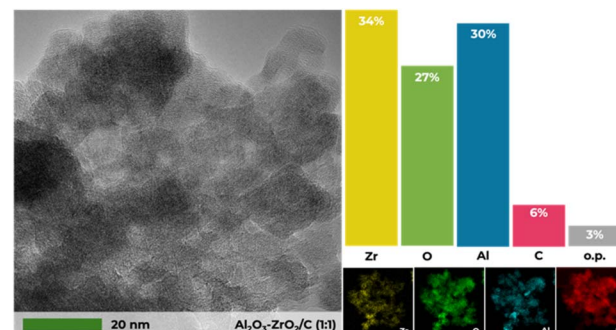


Fig. 5 STEM image and EDX analysis of the  $\text{Al}_2\text{O}_3$ – $\text{ZrO}_2/\text{C}$  (1 : 1) catalyst.

TEM analysis shows a homogeneous distribution of Zr and Al and distinctly captures the formation of  $\gamma$ - $\text{Al}_2\text{O}_3/\text{C}$ , with darker areas indicating particle presence (Fig. S3†), visually confirming its structural composition, and with lighter areas indicating the formation of  $\text{ZrO}_2$ . Scanning electron microscopy (SEM) was employed to further delineate the morphology of the materials. It reveals that the catalysts possess predominantly irregular, amorphous structures, either as blocks or planes. Notably, the  $\text{Al}_2\text{O}_3$ – $\text{ZrO}_2/\text{C}$  (1 : 1) sample exhibits a more porous structure compared to other materials, aligning with porosimetry results (Fig. S4†). Moreover, the EDS results presented in Fig. S5† confirm that the elemental ratios in  $\text{Al}_2\text{O}_3$ – $\text{ZrO}_2/\text{C}$  catalysts align with their respective nominal molar ratios, such as 2 : 1, 1 : 1 and 1 : 2.

### Catalytic test

To expedite catalyst screening and gain preliminary insights into the ability of MOF-derived  $\text{Al}_2\text{O}_3$ – $\text{ZrO}_2/\text{C}$  catalysts, all prepared systems were tested in the transfer hydrogenation of methyl levulinate by using 2-propanol as an indirect H-source at 200 °C at 30 min (Fig. 6).

The data presented in Fig. 6 point to the significant role of  $\text{Al}_2\text{O}_3$  content in modulating the catalytic efficiency of the examined systems.

Employing  $\text{ZrO}_2/\text{C}$  at 200 °C for 30 minutes resulted in an ML conversion rate of 24%, with a 100% selectivity towards GVL. The use of a pure  $\text{Al}_2\text{O}_3$  catalyst yielded a similar ML conversion rate of 20%, but with a significantly reduced GVL yield of 9%, where



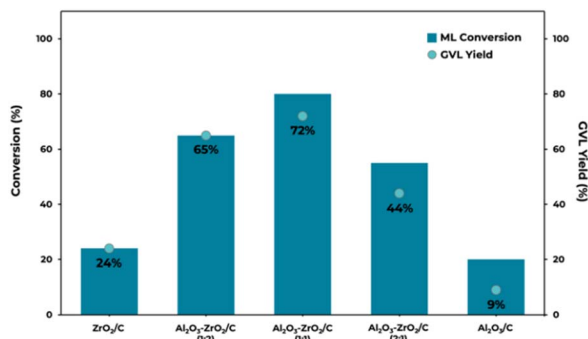


Fig. 6 Catalyst screening in the CTH of methyl levulinate into  $\gamma$ -valerolactone promoted by MOF-derived Al<sub>2</sub>O<sub>3</sub>-ZrO<sub>2</sub>/C catalysts by using 2-propanol as an H-source (reaction conditions: 0.5 mL min<sup>-1</sup> flow rate; ML 0.2 M in 2-propanol; 0.500 g of catalyst; 30 bar pressure; time on stream: 30 min; reaction temperature: 200 °C).

isopropyl levulinate (IPL) emerged as the predominant reaction product. When Al<sub>2</sub>O<sub>3</sub> was integrated in a 1:2 molar ratio with ZrO<sub>2</sub>, a notable enhancement in both ML conversion and GVL yield, peaking at 65%, was observed. This marked improvement suggests a synergistic interaction within the mixed metal oxide matrix, potentially augmenting the number and efficacy of catalytic sites available for the hydrogenation reaction.

The optimum catalytic performance was recorded with an equimolar ratio of Al<sub>2</sub>O<sub>3</sub> to ZrO<sub>2</sub> in the Al<sub>2</sub>O<sub>3</sub>-ZrO<sub>2</sub>/C (1:1) catalyst. This configuration not only enhanced ML conversion to an impressive 80% but also pushed GVL yield (72%). The GC-MS chromatogram of this reaction at 30 min time on stream is depicted in Fig. S6.†

To assess the catalytic efficiency, we quantified the productivity of  $\gamma$ -valerolactone (GVL) under specific conditions: employing 0.5 g of the Al<sub>2</sub>O<sub>3</sub>-ZrO<sub>2</sub>/C (1:1) catalyst at a flow rate of 0.5 mL min<sup>-1</sup>, with a reaction temperature of 200 °C and a N<sub>2</sub> pressure of 30 bar. The catalyst achieved a productivity rate of 9 mmol GVL per gram of catalyst per hour. This performance is noteworthy when compared with analogous systems such as ZrO<sub>2</sub>/SBA-15 and Zr-containing zeolites, which report productivities of 5.2 and 0.81 mmol GVL per gram of catalyst per hour, respectively.<sup>35-38,76</sup>

The performance data depict a tendency-curve where excessive addition of Al<sub>2</sub>O<sub>3</sub> beyond the optimum ratio led to a diminished conversion rate (55%) and a comparably reduced GVL yield (44%) when using Al<sub>2</sub>O<sub>3</sub>-ZrO<sub>2</sub>/C.

This trend can be attributed to the substantial surface area and the dense distribution of acidic and basic sites associated with the Al<sub>2</sub>O<sub>3</sub>-ZrO<sub>2</sub> ratio, where Al<sub>2</sub>O<sub>3</sub>-ZrO<sub>2</sub>/C (1:1) composition exhibits a higher density of acid (Table 2 and Fig. 2) and basic sites (Fig. 4). Moreover, it has been previously reported how basic sites contribute more importantly to the reaction than acid sites.<sup>77</sup> In other words, while Al<sub>2</sub>O<sub>3</sub> contributes beneficial properties to some extent, it may also induce over-adsorption and complex transformations of intermediates on the catalyst surface due to changes in the catalytic acid and basic sites. Additionally, an increase in the Al<sub>2</sub>O<sub>3</sub> content was correlated with a decreased GVL selectivity, favoring the production of isopropyl levulinate (IPL), a notable by-product.

Having identified Al<sub>2</sub>O<sub>3</sub>-ZrO<sub>2</sub>/C (1:1) as an optimum performing catalyst, subsequent experiments were focused to identify the best reaction conditions to maximize GVL production and to assess its practical application potential.

Temperature tests in the range from 160 °C to 220 °C were subsequently carried out to establish the optimum thermal conditions that favor high GVL yield while minimizing the formation of by-products such as isopropyl levulinate (IPL). Results revealed that temperatures above 200 °C resulted in a higher rate of ML conversion with decreased selectivity towards GVL, indicating a shift in reaction dynamics towards the IPL pathway (Fig. 7). These results already improve not only those obtained in continuous flows (Table 1), but also those obtained under batch conditions with similar materials subjected to high temperatures, pressures and times (Table S1†).

The time effect of Al<sub>2</sub>O<sub>3</sub>-ZrO<sub>2</sub>/C (1:1) in the transfer hydrogenation of methyl levulinate (ML) at 200 °C was meticulously monitored to assess changes in catalytic activity over prolonged time on stream (Fig. 8). By using the Al<sub>2</sub>O<sub>3</sub>-ZrO<sub>2</sub>/C (1:1) catalyst, a consistent decline in performance was observed over 6 hours of continuous reaction. Notably, a significant drop in activity commenced after the first 60 minutes with the investigated catalyst achieving a 75% ML conversion rate and a 67.5% GVL yield. As

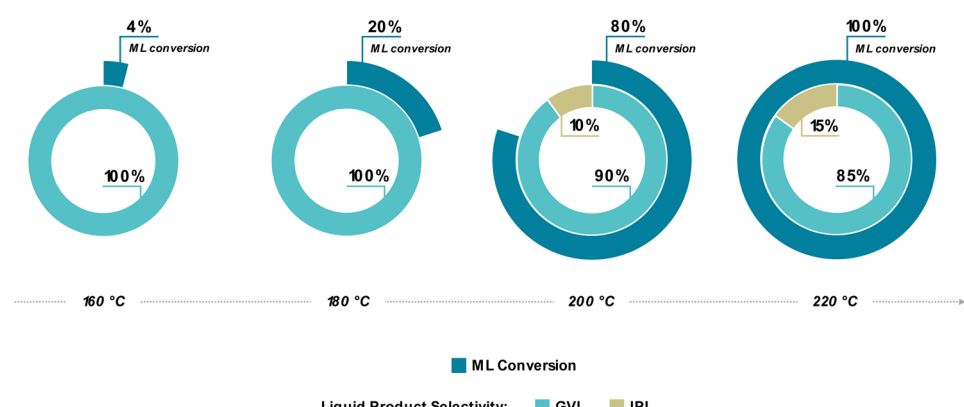


Fig. 7 Effect of reaction temperature on ML conversion and product selectivity for Al<sub>2</sub>O<sub>3</sub>-ZrO<sub>2</sub>/C (1:1) under transfer hydrogenolysis conditions (reaction conditions: 0.5 mL min<sup>-1</sup> flow rate; ML 0.2 M in 2-propanol; 0.500 g of catalyst; 30 bar pressure; time on stream: 30 min).



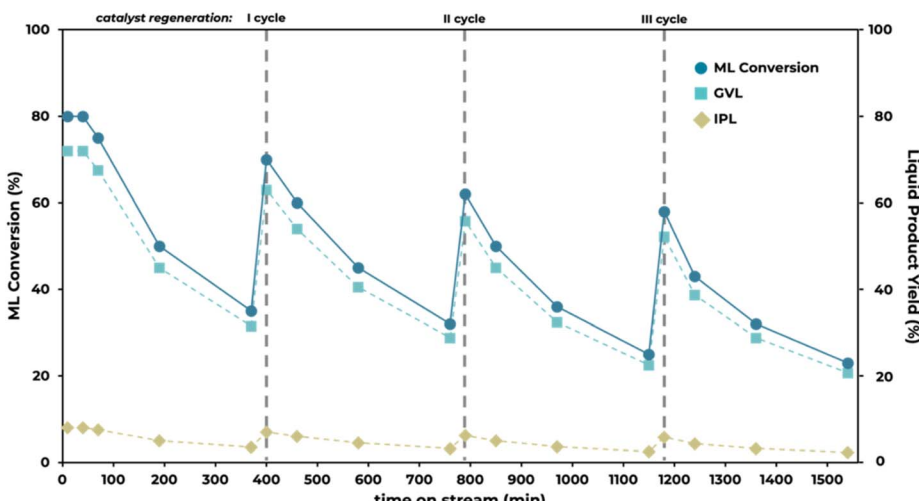


Fig. 8 CTH of methyl levulinate into  $\gamma$ -valerolactone promoted by the  $\text{Al}_2\text{O}_3\text{-ZrO}_2/\text{C}$  (1 : 1) catalyst against time (reaction conditions: 0.5  $\text{mL min}^{-1}$  flow rate; ML 0.2 M in 2-propanol; 0.500 g of catalyst; 30 bar pressure; reaction temperature: 200  $^{\circ}\text{C}$ ). The regeneration of the catalyst was performed for three consecutive cycles after 360 min of time-on-stream (dotted gray line).

the reaction progressed, ML conversion decreased to 35% and GVL yield to 31.5% by the end of 360 minutes. This decline in catalytic activity can primarily be attributed to the accumulation of humin deposits on the  $\text{Al}_2\text{O}_3\text{-ZrO}_2/\text{C}$  (1 : 1) catalyst surface, which block active sites and progressively deactivate the catalyst.

Other synthesized mixed oxide catalysts,  $\text{Al}_2\text{O}_3\text{-ZrO}_2$  (1 : 2) and  $\text{Al}_2\text{O}_3\text{-ZrO}_2$  (2 : 1), demonstrated similar deactivation patterns (Fig. S7†). This uniformity across different material compositions suggests that the presence of aluminum within the catalyst does not significantly impact catalytic stability. However, aluminum remains essential for optimizing both conversion and selectivity.

To address this challenge, a regeneration protocol was implemented. This involves halting the flow of the reagent mixture and removing the catalyst from the flow system. The catalyst is then subjected to a thermal treatment, where it is maintained at 400  $^{\circ}\text{C}$  in an air flow of 30  $\text{mL min}^{-1}$  for two hours. This procedure aimed to promote the combustion of deposited carbonaceous residues, effectively restoring its activity. It is important to emphasize that the regeneration treatment is not expected to alter the chemical nature or properties of the  $\text{Al}_2\text{O}_3\text{-ZrO}_2/\text{C}$  (1 : 1) catalyst. The catalyst underwent initial synthesis through a thermal treatment at 600  $^{\circ}\text{C}$ , a process far more intense than the subsequent regeneration at 400  $^{\circ}\text{C}$ . Consequently, the approximately 5% of carbon integrated into the material remains unchanged and is not oxidized into other species. Even in the unlikely event of oxidation, the minimal amount of carbon present would have negligible impact on the overall physico-chemical properties of the  $\text{Al}_2\text{O}_3\text{-ZrO}_2/\text{C}$  (1 : 1) catalyst.

Analysis of the catalyst performance after regeneration reveals a noticeable decline in ML conversion efficiency, yet the selectivity towards GVL remains consistently high at 90%. This demonstrates the catalyst's capability to maintain its effectiveness in producing the desired product despite a reduction in

overall activity. In comparison, when the catalyst is simply discharged and dried under normal conditions, it continues to function, yielding similar results to those observed during its last use. These results suggest that the catalyst's deactivation is primarily due to the blocking of active sites. Extensive literature indicates that in biomass processing, the deposition of humins (high-molecular-weight compounds formed by the polymerization of intermediates) on the catalytic surface is a major cause of catalyst deactivation.<sup>78-80</sup> Similarly, in this study, humins are primarily suspected as the main cause of deactivation. Although these compounds are not detectable by gas chromatography (GC) due to their high molecular weight, the carbon balance analysis, which shows a maximum weight loss of only 2%, suggests that a small portion of ML is converted into humins through a competing polymerization reaction.

The continuous flow setup intensifies this effect, as the catalyst sites are constantly exposed to the reaction mixture. Attempts to detect humins on the exhausted catalyst using ATR spectroscopy were unsuccessful due to the instrument's insufficient sensitivity to detect significant spectral differences. Additionally, the analysis of changes in acid-base sites was unreliable due to the temperature activation required prior to measurement, as detailed in the Experimental section. In any case, the correlation between the loss of active sites and humin deposition is supported not only by the observed catalytic behavior (where conversion decreases while selectivity remains constant, indicating that the remaining active sites are still functional) but also by the catalyst's color change to a slightly darker hue. Moreover, these observations align with corroborative findings from previous studies within our group on the reductive upgrading of biomass derived molecules under continuous flow conditions with oxide materials derived from MOFs, further validating our conclusions.<sup>47,81</sup>

Different flow rates were subsequently assessed employing  $\text{Al}_2\text{O}_3\text{-ZrO}_2/\text{C}$  (1 : 1) to investigate their effect on ML conversion



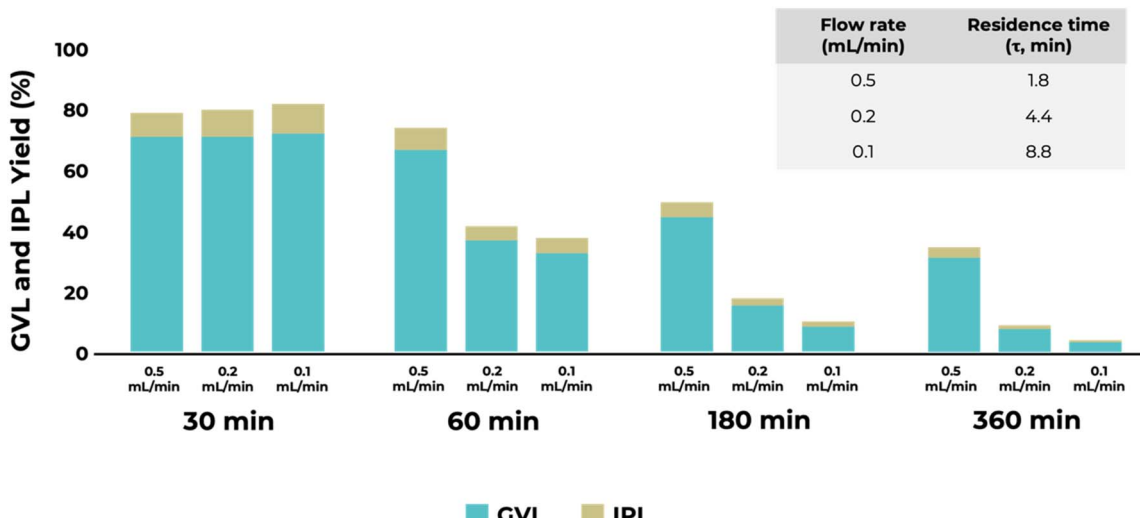
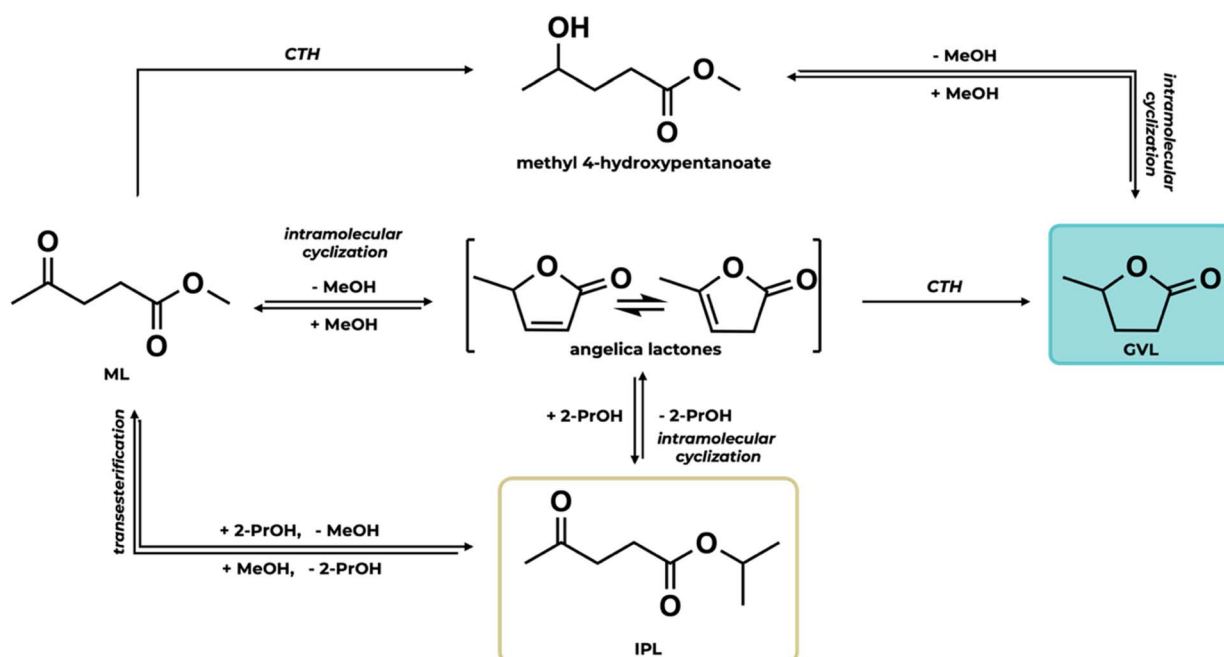


Fig. 9 CTH of methyl levulinate into *g*-valerolactone promoted by  $\text{Al}_2\text{O}_3\text{-ZrO}_2/\text{C}$  (1 : 1) under a flow rate effect at different times on stream (reaction conditions: ML 0.2 M in 2-propanol; 0.500 g of catalyst; 30 bar pressure; reaction temperature: 200 °C).

and GVL yield at 200 °C. Results, including the residence time for each condition, are depicted in Fig. 9.

Initially, at 30 minutes, reducing the flow rates from 0.5  $\text{mL min}^{-1}$  to 0.2  $\text{mL min}^{-1}$  and 0.1  $\text{mL min}^{-1}$  did not significantly influence ML conversion rates (80%, 81% and 83%, respectively at 0.5, 0.2 and 0.1  $\text{mL min}^{-1}$ ) or GVL selectivity (90% at 0.5, 88.9% at 0.2  $\text{mL min}^{-1}$  and 88% at 0.1  $\text{mL min}^{-1}$ ). However, by using a lower flow rate, catalyst deactivation was markedly accelerated, evidenced by the significant drop in ML conversion to 4% at a lower flow rate of 0.1  $\text{mL min}^{-1}$  after 360 minutes, likely due to prolonged contact between the reactants and the catalyst, as demonstrated by the increased residence time. This prolonged

contact time also shifted product selectivity, primarily increasing the tendency for ML to undergo transesterification and likely leading to the deposition of humins on the catalyst surface at lower residence times. As a result, GVL selectivity decreased progressively over time, from 88.9%, 88.5%, and 86%, to 85% at 0.2  $\text{mL min}^{-1}$  and from 88%, 86.7%, and 84.4%, to 82.8% at 0.1  $\text{mL min}^{-1}$  for 30-, 60-, 180-, and 360 minutes of time on stream, respectively. Conversely, at a higher flow rate of 1  $\text{mL min}^{-1}$ , the system encountered complications such as blockages. This outcome emphasizes the importance of balancing contact time to maintain both the effectiveness and durability of the catalytic system as well as to prevent mechanical issues.



Scheme 2 Reaction pathways in the CTH of methyl levulinate (ML) with 2-propanol to GVL under continuous flow conditions.



## Understanding of GVL production pathways in the presence of 2-propanol

The conversion of methyl levulinate (ML) into  $\gamma$ -valerolactone (GVL) *via* a transfer hydrogenation process is thoroughly documented and remains a focus of significant research interest.<sup>12,13,82-84</sup> Utilizing 2-propanol both as a solvent and a hydrogen donor, ML is subjected to a variety of chemical transformations that may lead to GVL production. These transformations are primarily categorized into three potential pathways (Scheme 2):

(1) Direct (transfer) hydrogenation: the carbonyl group in ML is first CTH hydrogenated through catalytic transfer hydrogenation (CTH), leading to the formation of methyl 4-hydroxy-pentanoate that is then rapidly cyclized into GVL.

(2) Cyclization and subsequent (transfer) hydrogenation: ML might initially cyclize into various lactone intermediates, which are subsequently hydrogenated to produce GVL.

(3) ML undergoes transesterification with 2-propanol, resulting in the formation of isopropyl levulinate (IPL) that can be further converted into GVL *via* lactone cyclization.

Catalytic tests and physicochemical characterizations facilitate the interpretation of reported results and support the hypothesized mechanisms underlying GVL production. Results related to the effects of temperature and alumina content distinctly show that introducing alumina into the catalyst system significantly influences the course of these reactions. The presence of alumina notably enhances ML conversion, while its varying content critically impacts substrate conversion and liquid product selectivity. Notably, an increased Al/Zr ratio tends to increase ML conversion and alters the reaction pathway, especially under elevated temperatures (220 °C).

Experimental outcomes reveal that lower reaction temperatures (up to 180 °C) and a minimum presence of alumina (up to a 1:1 Al/Zr ratio) favor the activation of 2-propanol, thereby promoting transfer hydrogenation reactions over transesterification, which in turn directs product selectivity towards enhanced GVL production. Conversely, higher alumina content and increased reaction temperatures tend to favor intramolecular cyclization, predominantly leading to the formation of IPL. In any case, the absence of detectable methyl 4-hydroxy-pentanoate and lactone intermediates in experimental analyses restricts a definitive conclusion about whether GVL is primarily produced from the direct hydrogenation (pathway 1) or *via* cyclization and subsequent hydrogenation (pathway 2).

## Conclusions

The effectiveness of MOF-derived Al<sub>2</sub>O<sub>3</sub>-ZrO<sub>2</sub>/C catalysts in the catalytic transfer hydrogenation of methyl levulinate to  $\gamma$ -valerolactone under continuous flow conditions was successfully demonstrated. By incorporating Al<sub>2</sub>O<sub>3</sub> into ZrO<sub>2</sub> using MOFs as sacrificial templates, the catalytic performance was significantly enhanced due to the synergistic interaction between these two oxides. The combination of alumina and zirconia in catalysts not only enhances the number of acid and base sites but also increases the specific surface areas of the

resulting catalysts. Notably, all mixed Al-Zr oxides demonstrated superior catalytic activity compared to the individual ZrO<sub>2</sub> and Al<sub>2</sub>O<sub>3</sub> catalysts, with the Al<sub>2</sub>O<sub>3</sub>-ZrO<sub>2</sub>/C catalyst with a 1:1 ratio demonstrating superior performance, achieving more than 99% conversion of ML and 85% yield of GVL at 220 °C within 30 minutes.

Optimum reaction conditions were identified to maximize GVL production, with a reaction temperature of 200 °C and a duration of 30 minutes proving most effective. These conditions effectively balanced the catalytic activity, leading to high conversion rates and desired product yields. Extended time on stream up to 6 hours showed a decrease in ML conversion and GVL yield, primarily due to catalyst deactivation from carbonaceous deposits. However, thermal regeneration at 400 °C successfully restored the catalyst's activity, demonstrating the feasibility of catalyst reuse.

The study also highlights the importance of maintaining balanced Al/Zr ratios to optimize selectivity and avoid excessive production of by-products such as isopropyl levulinate (IPL) through transesterification reactions. Different flow rates were tested, and the optimal flow rate was determined to be 0.5 mL min<sup>-1</sup>, which maintained high conversion and selectivity while preventing catalyst deactivation.

The successful implementation of a thermal regeneration strategy additionally underscores the potential practical feasibility of this catalytic system for industrial applications. To further enhance the promise of this work and align with sustainable development goals, we have already begun to focus on two crucial advancements: (i) the synthesis of MOF-derived materials utilizing greener aprotic solvents, and (ii) the refinement of catalyst synthesis conditions to not only preserve but also optimize the high selectivity observed while improving stability and thereby increasing GVL production. Since  $\gamma$ -valerolactone (GVL) is one of the most promising chemicals in modern biorefineries, these enhancements in its catalytic production from methyl-levulinate are anticipated to significantly advance the development of a circular economy, optimizing resource efficiency and minimizing waste.

## Data availability

The data supporting this article have been included as part of the ESI.<sup>†</sup>

## Author contributions

Marina Ronda-Leal: writing – review & editing, writing – original draft, methodology, investigation, formal analysis, data curation. Alina M. Balu: visualization, investigation. Rafael Luque: visualization, investigation, resources, project administration, funding acquisition. Francesco Mauriello: writing – review & editing, visualization, methodology, investigation. Alberto Ricchibuno: writing – review & editing, methodology, investigation. Christophe Len: visualization, investigation. Antonio A. Romero: writing – review & editing, validation, supervision, resources, project administration. Emilia Paone: writing – review & editing, validation, supervision, conceptualization.



## Conflicts of interest

The authors declare that they have no known conflicts of interest that could have appeared to influence the work reported in this paper.

## Acknowledgements

This publication was prepared with support and funding from the European Union – NextGenerationEU under the Italian Ministry of University and Research (MUR) National Innovation Ecosystem grant “Ecosistema TECH4YOU” (CUP: C33C22000290006, Spoke 3 – Goal 3.5). Emilia Paone gratefully acknowledges the Italian Ministry for University and Research (MUR) and the Università degli Studi Mediterranea di Reggio Calabria for funding under D.M. 1062/2021 and D.M. 737/2022 programs. A.A. Romero gratefully acknowledges MINECO for funding under project PID2019-109953GB-100, co-financed with FEDER funds. M. Ronda Leal also expresses gratitude to the MINECO project for providing an FPU contract (REF: FPU20/03875) associated with the PID2019-109953GB-100 project, carried out within the FQM-383 Group. The authors express their gratitude to the anonymous reviewers for their insightful comments and feedback, which have significantly enhanced the quality of the paper.

## References

- 1 M. Ishaq, G. Ghose, R. Fernandez-Gonzalez, F. Puime-Guillen, N. Tandir and H. M. S. de Oliveira, *Front. Environ. Sci. Eng.*, 2022, **10**, 941791.
- 2 United Nations, *COP28 Ends with Call to ‘Transition Away’ from Fossil Fuels; UN Chief Says Phaseout Inevitable*, <https://unsdg.un.org/latest/stories/cop28-ends-call-%E2%80%99transition-away%E2%80%99-fossil-fuels-un-chief-says-phaseout-inevitable>, accessed 2024-06-12.
- 3 L. Hens, C. Block, J. J. Cabello-Eras, A. Sagastume-Gutierrez, D. Garcia-Lorenzo, C. Chamorro, K. Herrera Mendoza, D. Haeseldonckx and C. Vandecasteele, *J. Cleaner Prod.*, 2018, **172**, 3323–3333.
- 4 S. Abate, G. Centi and S. Perathoner, *Natl. Sci. Rev.*, 2015, **2**, 143–145.
- 5 M. E. Boot-Handford, J. C. Abanades, E. J. Anthony, M. J. Blunt, S. Brandani, N. Mac Dowell, J. R. Fernández, M.-C. Ferrari, R. Gross, J. P. Hallett, R. S. Haszeldine, P. Heptonstall, A. Lyngfelt, Z. Makuch, E. Mangano, R. T. J. Porter, M. Pourkashanian, G. T. Rochelle, N. Shah, J. G. Yao and P. S. Fennell, *Energy Environ. Sci.*, 2014, **7**, 130–189.
- 6 E. Paone, T. Tabanelli and F. Mauriello, *Curr. Opin. Green Sustainable Chem.*, 2020, **24**, 1–6.
- 7 C. Xu, E. Paone, D. Rodríguez-Padrón, R. Luque and F. Mauriello, *Renewable Sustainable Energy Rev.*, 2020, **127**, 109852.
- 8 C. Espro, E. Paone, F. Mauriello, R. Gotti, E. Uliassi, M. L. Bolognesi, D. Rodríguez-Padrón and R. Luque, *Chem. Soc. Rev.*, 2021, **50**, 11191–11207.
- 9 A. Satira, E. Paone, V. Bressi, D. Iannazzo, F. Marra, P. S. Calabro, F. Mauriello and C. Espro, *Appl. Sci.*, 2021, **11**, 10983.
- 10 E. Paone, M. Miceli, A. Malara, G. Ye, E. Mousa, E. Bontempi, R. Pietropaolo and F. Mauriello, *ACS Sustainable Chem. Eng.*, 2022, **10**, 2275–2281.
- 11 E. Paone, F. Fazzino, D. M. Pizzone, A. Scurria, M. Pagliaro, R. Ciriminna and P. S. Calabro, *Sustainability*, 2021, **13**, 2428.
- 12 T. Tabanelli, E. Paone, P. B. Vásquez, R. Pietropaolo, F. Cavani and F. Mauriello, *ACS Sustainable Chem. Eng.*, 2019, **7**, 9937–9947.
- 13 P. B. Vásquez, T. Tabanelli, E. Monti, S. Albonetti, D. Bonincontro, N. Dimitratos and F. Cavani, *ACS Sustainable Chem. Eng.*, 2019, **7**, 8317–8330.
- 14 L. e, Y. Han, J. Feng and X. Lu, *Ind. Crops Prod.*, 2020, **144**, 112031.
- 15 M. G. Al-Shaal, M. Calin, I. Delidovich and R. Palkovits, *Catal. Commun.*, 2016, **75**, 65–68.
- 16 A. S. Amarasekara and M. A. Hasan, *Catal. Commun.*, 2015, **60**, 5–7.
- 17 L. Biancalana, S. Fulignati, C. Antonetti, S. Zacchini, G. Provinciali, G. Pampaloni, A. M. Raspolli Galletti and F. Marchetti, *New J. Chem.*, 2018, **42**, 17574–17586.
- 18 D. Wang and D. Astruc, *Chem. Rev.*, 2015, **115**, 6621–6686.
- 19 M. J. Gilkey and B. Xu, *ACS Catal.*, 2016, **6**, 1420–1436.
- 20 C. Espro, B. Gumina, T. Szumelda, E. Paone and F. Mauriello, *Catalysts*, 2018, **8**, 313.
- 21 A. Démolis, N. Essayem and F. Rataboul, *ACS Sustainable Chem. Eng.*, 2014, **2**, 1338–1352.
- 22 T. Komanoya, K. Nakajima, M. Kitano and M. Hara, *J. Phys. Chem. C*, 2015, **119**, 26540–26546.
- 23 Y. Kuwahara, W. Kaburagi, Y. Osada, T. Fujitani and H. Yamashita, *Catal. Today*, 2017, **281**, 418–428.
- 24 S. Ostovar, H. Saravani and D. Rodríguez-Padrón, *Renewable Energy*, 2021, **178**, 1070–1083.
- 25 M. Chia and J. A. Dumesic, *Chem. Commun.*, 2011, **47**, 12233–12235.
- 26 M. Boronat, A. Corma and M. Renz, *J. Phys. Chem. B*, 2006, **110**, 21168–21174.
- 27 A. Osatiashvili, A. F. Lee and K. Wilson, *J. Chem. Technol. Biotechnol.*, 2017, **92**, 1125–1135.
- 28 X. Chen, T. Zhao, X. Zhang, Y. Zhang, H. Yu, Q. Lyu, X. Jia, L. Han and W. Xiao, *J. Energy Chem.*, 2021, **63**, 430–441.
- 29 R. Q. Raguindin and J. G. Seo, *Chem. Eng. J.*, 2024, 152141.
- 30 N. Karanwal, D. Verma, P. Butolia, S. M. Kim and J. Kim, *Green Chem.*, 2020, **22**, 766–787.
- 31 M. B. Gawande, R. K. Pandey and R. V. Jayaram, *Catal. Sci. Technol.*, 2012, **2**, 1113–1125.
- 32 J. C. Védrine, *Catalysts*, 2017, **7**, 341.
- 33 C. García-Sancho, C. P. Jiménez-Gómez, N. Viar-Antuño, J. A. Cecilia, R. Moreno-Tost, J. M. Mérida-Robles and P. Maireles-Torres, *Appl. Catal. A*, 2021, **609**, 117905.
- 34 J. He, H. Li, Y. M. Lu, Y. X. Liu, Z. B. Wu, D. Y. Hu and S. Yang, *Appl. Catal. A*, 2016, **510**, 11–19.
- 35 T. Tabanelli, P. B. Vásquez, E. Paone, R. Pietropaolo, N. Dimitratos, F. Cavani and F. Mauriello, *Chem. Proc.*, 2020, **2**, 28.



36 W. Ouyang, D. Zhao, Y. Wang, A. M. Balu, C. Len and R. Luque, *ACS Sustain. Chem. Eng.*, 2018, **6**, 6742–6756.

37 D. Zhao, Y. Wang, F. Delbecq and C. Len, *Mol. Catal.*, 2019, **475**, 110456.

38 M. Cabanillas, A. Franco, N. Lázaroa, A. M. Balua, R. Luque and A. Pineda, *Mol. Catal.*, 2019, **477**, 110522.

39 D.-P. Phan, M. H. Tran and E. Y. Lee, *Mater. Today Chem.*, 2023, **33**, 101691.

40 A. Kumari, S. Kaushal and P. P. Singh, *Mater. Today Energy*, 2021, **20**, 100667.

41 X. Liu, Z. Liu and R. Wang, *Adv. Polym. Technol.*, 2020, **2020**, 1201923.

42 J. Gascon, A. Corma and F. Kapteijn, *ACS Catal.*, 2014, **4**, 361–378.

43 R. Fang, A. Dhakshinamoorthy and Y. Li, *Chem. Soc. Rev.*, 2020, **49**, 3638–3687.

44 Q. Fu, H. Jiang, Y. Wang, H. Wang and X. Zhao, *Mater. Chem. Front.*, 2023, **7**, 628–642.

45 W. Ouyang, D. Zhao, Y. Wang, A. M. Balu, C. Len and R. Luque, *ACS Sustainable Chem. Eng.*, 2018, **6**, 6746–6752.

46 J. Li, S. Zhao, Z. Li, D. Liu, Y. Chi and C. Hu, *Inorg. Chem.*, 2021, **60**, 7785–7793.

47 M. Ronda-Leal, S. M. Osman, H. W. Jang, M. Shokouhimehr, A. A. Romero and R. Luque, *Fuel*, 2023, **333**, 126221.

48 H. Furukawa, K. E. Cordova, M. O'Keeffe and O. M. Yaghi, *Science*, 2013, **341**, 1230444.

49 A. Dhakshinamoorthy, S. Navalon, A. M. Asiri and H. Garcia, *Chem. Commun.*, 2020, **56**, 26–45.

50 S. L. Griffiths, P. Boyall, J. P. Müller, A. M. Harrington, W. Sobolewska, W. R. Reynolds, A. B. Richard, K. Wu, S. M. Collins, M. Muldowney and T. W. Chamberlain, *Nanoscale*, 2023, **15**, 17910–17921.

51 M.-L. Hu, M. Y. Masoomi and A. Morsali, *Coord. Chem. Rev.*, 2019, **387**, 415–435.

52 K.-Y. Zou and Z.-X. Li, *Chem. - Eur. J.*, 2018, **24**, 6506–6518.

53 W. Cao, W. Luo, H. Ge, Y. Su, A. Wang and T. Zhang, *Green Chem.*, 2017, **19**, 2201–2211.

54 W. Cao, L. Lin, H. Qi, Q. He, Z. Wu, A. Wang, W. Luo and T. Zhang, *J. Catal.*, 2019, **373**, 161–172.

55 C. Van Nguyen, B. M. Matsagar, J.-Y. Yeh, W.-H. Chiang and K. C.-W. Wu, *J. Mol. Catal.*, 2019, **475**, 110478.

56 R. J. McKinstry, E. J. Cathcart Cussen, A. J. Fletcher, S. V. Patwardhan and J. Sefcik, *Chem. Eng. J.*, 2016, **285**, 718–725.

57 N. J. A. Rahman, A. Ramli, K. Jumbri and Y. Uemura, *Sci. Rep.*, 2019, 16223.

58 J. Sakfali, S. B. Chaabene, R. Akkari, F. Dappozze, G. Berhault, C. Guillard and M. S. Zina, *J. Photochem. Photobiol. A*, 2022, **430**, 113970.

59 C. Guo, P. Wang, S. Liao, H. Si, S. Chen, G. Fan and Z. Wang, *Appl. Sci.*, 2019, **9**(19), 4145.

60 M. Farrag, *Sci. Rep.*, 2023, **13**, 10123.

61 S. Shi, S. Qian, X. Hou, J. Mu, J. He and X. Chou, *Adv. Condens. Matter Phys.*, 2018, **1**, 7598978.

62 N. Tao, J. Liu, Y. Xu, Y. Feng, Y. Wang, W. Liu and J. Lv, *Chem. Pap.*, 2020, **74**, 3503–3515.

63 C. Liu, J. Sun, H. M. Brown, O. G. Marin-Flores, J. T. Bays, A. M. Karim and Y. Wang, *Catal. Today*, 2016, **269**, 103–109.

64 J. He, H. Li, Y.-M. Lu, Y.-X. Liu, Z.-B. Wu, D.-Y. Hu and S. Yang, *Appl. Catal. A*, 2016, **510**, 11–19.

65 H. Bekhti, Y. Boucheffa, A. H. A. Blal and A. Travert, *Vib. Spectrosc.*, 2021, **117**, 103313.

66 J. Goscianska, M. Ziolek, E. Gibson and M. Daturi, *Catal. Today*, 2010, **152**(1–4), 33–41.

67 V. Bolis, G. Magnacca, G. Cerrato and C. Morterra, *Thermochim. Acta*, 2001, **379**(1–2), 147–161.

68 K. Pokrovski, K. T. Jung and A. T. Bell, *Langmuir*, 2001, **17**(14), 4297–4303.

69 C. Morterra, A. Zecchina, S. Coluccia and A. Chiorino, *J. Chem. Soc., Faraday Trans.*, 1977, **71**(73), 1544–1560.

70 H. Y. T. Chen, S. Tosoni and G. Pacchioni, *Surf. Sci.*, 2016, **652**, 163–171.

71 J. Podobiński and J. Datka, *Molecules*, 2024, **29**(8), 1726.

72 S. Mukhopadhyay, R. Shimoni, I. Liberman, R. Ifraimov, I. Rozenberg and I. Hod, *Angew. Chem.*, 2021, **133**, 13535–13541.

73 X. Chen, X. Liu, L. Zhu, X. Tao and X. Wang, *Chemosphere*, 2022, **291**, 133032.

74 Z. Dai, D. T. Lee, K. Shi, S. Wang, H. F. Barton, J. Zhu, J. Yan, Q. Ke and G. N. Parsons, *J. Mater. Chem. A*, 2020, **8**, 3803–3813.

75 M. A. Gondal, T. A. Fasasi, U. Baig and A. Mekki, *J. Nanosci. Nanotechnol.*, 2018, **18**, 4030–4039.

76 A. Osatiashvili, S. A. Orr, L. J. Durnell, I. Collado García, A. Merenda, A. F. Lee and K. Wilson, *Catal. Sci. Technol.*, 2022, **12**, 5611.

77 Y. Kuwahara, H. Kango and H. Yamashita, *ACS Sustainable Chem. Eng.*, 2017, **5**(1), 1141–1152.

78 G. Caeiro, J. M. Lopes, P. Magnoux, P. Ayrault and F. R. Ribeiro, *J. Catal.*, 2007, **249**, 234–243.

79 D. G. Blackmond, J. G. Goodwin and J. E. Lester, *J. Catal.*, 1982, **78**, 34–43.

80 J. V. Ibarra, C. Royo, A. Monzón and J. Santamaría, *Vib. Spectrosc.*, 1995, **9**(2), 191–196.

81 M. Ronda-Leal, N. Lázaro, A. Pineda, A. A. Romero and R. Luque, *Sustainable Chem. Pharm.*, 2024, **38**, 101467.

82 M. Cabanillas, A. Franco, N. Lázaro, A. M. Balu, R. Luque and A. Pineda, *Mol. Catal.*, 2019, **477**, 110522.

83 M. Douthwaite, B. Zhang, S. Iqbal, P. J. Miedziak, J. K. Bartley, D. J. Willock and G. J. Hutchings, *Catal. Commun.*, 2022, 106430.

84 M. Ma, X. Yan, P. Hou, J. Cao, H. Liu, X. Xu, H. Yue, G. Tian, S. Jing and S. Feng, *ChemistrySelect*, 2020, **5**, 924–930.

